Evaluation of neural network emulations for radiation parameterization in cloud resolving model

Soonyoung Roh and Hwan-Jin Song*

National Institute of Meteorological Sciences, Korea Meteorological Administration, Jeju-do, Republic of Korea

Submitted to Geophysical Research Letters

(June 2020)

* *Corresponding author's address*
Hwan-Jin Song
National Institute of Meteorological Sciences,
63568, Seogwipo-si, Jeju-do, Republic of Korea
E-mail: hwanjinsong@gmail.com
Phone: +82-64-780-6758

Abstract

This study evaluated the forecast performance of neural network (NN)-based radiation emulators with 300 and 56 neurons developed under the cloud-resolving simulation. These emulators are 20–100 times cheaper to employ than the original parameterization and express evolutionary features well for 6 hrs. The results suggest that the frequent use of an NN emulator can improve not only computational speed but also forecasting accuracy in comparison to the infrequent use of original radiation parameterization, which is commonly used for speedup but can induce numerical instability as a result of imbalance with other processes. The forecast error of the emulator results was much improved in comparison with that for infrequent radiation runs with similar computational cost. The 56-neuron emulator results were even more accurate than the infrequent runs, which had a computational cost five times higher. The speed and accuracy advantages of radiation emulators can be utilized for weather forecasting.

Key Points

- A neural network (NN)-based radiation emulator was developed and evaluated at a cloud-resolving scale.
- Radiation emulators with 300 and 56 neurons are 20–100 times faster than the original scheme.
- Frequent emulator results can be more accurate than infrequent calculations of original radiation scheme.

Plain Language Summary

Radiative transfer calculations in weather and climate models often impose computational challenges because of the complexity of radiation processes. Neural network (NN)-based emulators have been developed to mimic radiation parameterization while reducing the computational time requirements and costs involved. However, no one has provided a standard for evaluating the performance of the emulator in terms of both speed and accuracy. The emulators developed in this study reduce the computational time required by factors of 20–100 while maintaining reasonable forecast accuracy. The use of such emulators is beneficial in terms of both computational speed and accuracy, in comparison to conventional infrequent use of radiation parameterization. The speed and accuracy advantages of NN-based radiation emulators make them useful for weather forecasting.

1. Introduction

Radiation is a fundamental energy source that drives weather and climate systems, so appropriate representation of radiative processes plays an important role in weather and climate prediction. The direct approach using a line-by-line radiative model (e.g., Clough et al., 1992 and 2005), can compute radiation processes precisely but is prohibitively expensive. To address the computational cost, numerical weather/climate prediction models that employ approximate radiation parameterization (e.g., Iacono et al., 2008; Gu et al., 2011; Baek, 2017) have been developed and heuristically turned to the line-by-line model. Radiation parameterization is still computationally expensive, compared to other schemes, because of the complexity of the underlying physical system. To circumvent the computational cost, radiation parameterizations have been computed less often than the time step of weather prediction model. However, this approach can lead to significant error in accumulated discrepancies in interaction with other dynamic/physical processes over time (Xu and Randall, 1995; Pauluis and Emanuel, 2004; Pincus and Stevens, 2013).

The necessity of a trade-off between speed and accuracy in radiation calculations has resulted in the search for alternative approaches, such as data-driven radiation emulator based on neural networks (NN) which achieves considerable improvement in speed with reasonable accuracy. Chevallier et al. (1998 and 2000) first developed NN-based longwave radiation emulators for the European Centre for Medium-Range Weather Forecasts (ECMWF) models. The NN-based longwave/shortwave emulators have been also developed for the Community Atmosphere Model (CAM), the Climate Forecast System (CFS), and the Super-Parameterized Energy Exascale Earth System Model (SP-E3SM) in various studies (Krasnopolsky et al., 2005; Krasnopolsky and Fox-Rabinovitz, 2006; Krasnopolsky et al., 2008a and 2008b; Krasnopolsky et al., 2010; Belochitski et al., 2011; Pal et al., 2019; Boukabara et al., 2019). Krasnopolsky et al. (2010) presented impressive results for an

93 emulator for the Rapid Radiative Transfer Model for General Circulation Models (RRTMG;
94 Clough et al., 2005 and Iacono et al., 2008), which improved computational speed by 16–60
95 times in comparison to the original scheme, while preserving long-term (17-yr) stability. Pal
96 et al. (2019) achieved a tenfold improvement in computational speed and 90–95% accuracy
97 using a deep neural network (DNN), indicating a greater computational burden in the case of
98 DNN. Similarly, various emulators have been developed for idealized frameworks (e.g.,
99 Krasnopolsky et al., 2013, Brenowitz and Bretherton, 2018; Rasp et al., 2018) as well as for
100 convection (Gentine et al., 2018), the planetary boundary layer (Wang et al., 2019), dynamics
101 (Scher, 2018).

102 Previously developed radiation emulators were applied to climate simulations at coarse
103 temporal (1–3 hr) and horizontal (100–300 km) resolutions. Although Pal et al. (2019) tried
104 to develop the radiation emulator under the super-parameterized cloud simulation; it is not
105 pure cloud-resolving simulation with high nonlinearity because they applied the results to 1-
106 degree horizontal resolution. The performance evaluation of emulator under the cloud-
107 resolving scale (i.e., less than a few km) is essential to be applied to weather forecasting
108 models. Furthermore, all radiation emulator studies did not provide quantitative criteria for
109 evaluating the accuracy of emulator, though they provided statistical similarity to the original
110 radiation parameterization on a climatic scale. However, because the infrequent use of
111 radiation scheme with a substantial speedup is often for rapid forecasting in meso-scale
112 weather prediction models, the radiation emulator is meaningful in weather forecasting when
113 it gives benefits both in speedup and accuracy in comparison to the conventional infrequent
114 radiation runs.

115 Therefore, this study sought to evaluate the accuracy improvement achieved with a
116 frequently used radiation emulator in comparison to the infrequent original scheme with
117 similar computation cost under the idealized cloud-resolving framework. This evaluation

approach is strongly recommended for the future development of radiation emulators. To achieve this goal, we developed an NN-based emulator for radiation parameterization for use with the Korea Local Analysis and Prediction System (KLAPS; Kim et al., 2002), which is an operational short-range weather forecast model used by the Korea Meteorological Administration (KMA). Although this study only involved evaluations in an ideal environment, it is expected that application of the proposed method to actual weather forecasting will yield many advantages in terms of speedup and accuracy.

2. Training Data and Methods

A two-dimensional idealized squall line simulation was performed with KLAPS, which is based on the Advanced Research Weather Research and Forecasting (WRF-ARW) model. This is a popular cloud simulation for development of microphysics schemes, as well as for understanding cloud-precipitation processes (e.g., Lim and Hong, 2010; Song et al., 2017; Bae et al., 2019). In this experiment, we considered the RRTMG-K radiation (Baek, 2017) and WRF Double Moment 7-Class (WDM7) microphysics (Bae et al., 2019) schemes, which are available in WRF version 4.1. The RRTMG-K scheme, a two-stream correlated-k approach, optimizes a Monte Carlo independent column approximation and calculates radiative fluxes and heating rates over the longwave (LW) with 140-g points for 16 bands (within 820–50000 cm^{-1}) and shortwave (SW) with 112-g points for 14 bands (within 10–3000 cm^{-1}). The control run was integrated at every model/radiation time step, every 3 s, on 201 horizontal grids (at 0.25-km intervals) and 39 vertical layers (up to 50 hPa) for 6-hr periods (from noon to sunset), which is equivalent to half of a daytime solar cycle. Note that the squall line experiment is suitable for up to 7 hrs of simulation (e.g., Lim and Hong, 2010, Bae et al., 2019). The RRTMG-K scheme is responsible for 86.47% of the total computation cost in the current simulation and is 9% faster than the RRTMG.

143 The training sets used to develop the NN-emulator were random samples of 20% of a full
144 data set from the control run. Although part of the control run included the training sets, this
145 study was focused on a limited framework for cloud simulation rather than on developing a
146 general NN-emulator. The NN-emulator inputs for RRTMG-K (196) are as follows: vertical
147 pressure, temperature, water vapor, ozone, cloud fraction, surface temperature, solar constant
148 (G), cosine solar zenith angle (cos θ), and forecast time (i.e., accumulated time steps). The
149 microphysics variables (cloud liquid/ice/snow effective radius and water path) were excluded
150 from the input data for the purpose of increasing the computational speed, although coupling
151 between radiation and microphysics schemes was inherently allowed (Bae et al., 2016; Bae
152 and Park, 2019), and thus cloud effects were expressed only by cloud fraction. The inclusion
153 of microphysics variables did not significantly improve accuracy, despite doubling
154 computational cost in comparison to the developed NN-emulator (not shown). The outputs
155 (86) consist of heating rate profiles for the LW and SW, as well as six LW and two SW
156 fluxes. For the LW fluxes, there were total/clear sky upward fluxes at the top of the
157 atmosphere (TOA) and the surface, respectively, and total/clear sky downward fluxes at the
158 surface. Total sky upward SW fluxes at the TOA and surface were also considered. However,
159 the total/clear sky downward SW fluxes at the TOA were directly expressed by $G \times \cos\theta$,
160 and clear sky upward SW fluxes at the TOA and surface were expressed by linear regressions
161 with respect to $G \times \cos\theta$ because of their strong dependency on the solar cycle. The
162 total/clear sky downward SW fluxes at the surface were replaced by total/clear sky upward
163 SW fluxes divided by a constant surface albedo (0.2). These replaced components should be
164 included in real-case simulations in the future. Additional redundant constant variables (e.g.,
165 trace gases and aerosols) were excluded to avoid additional noise in advance.
166 The single-layer NN method described by Krasnopolsky et al. (2010) was used in this
167 study to develop the RRTMG-K emulator. For any given inputs, the NN-emulator provides

approximated outputs without the use of the complex processes in the original parameterization. The approximating function (Eq. 1) and related coefficients are learned from the training sets.

$$Y_q = B2_q + \sum_{j=1}^{k} W2_{qj} \cdot \tanh(B1_j + \sum_{i=1}^{n} W1_{ji} \cdot X_i) \quad (1)$$

Here, n and m indicate the number of inputs and outputs; X_i denotes the input and output vectors; Y_q is the predicted output vector for q=1,2,…, m; W1 and W2 are the matrices of the weights from input to hidden layers [n, k] and from hidden to output layers [k, m], respectively; B1 and B2 indicate the bias vectors from input to hidden layers and hidden to output layers, respectively; and tanh is used for the nonlinear activation function. The accuracy of NN emulation can be tuned by increasing the number of hidden neurons (k), whereas its speedup is inversely proportional to the numerical complexity; k×(n+m+1)+m, as given by Krasnopolsky et al. (2010). The values obtained for the coefficients (W1, W2, B1, and B2) are implemented in the NN-emulator. The NN-emulator replaces combined LW and SW radiations all at once, not separately, and hence, it has an advantage in speedup related to the reduction of the W1 and B1 arrays, because LW and SW radiation share the majority of inputs. The NN-emulators with 300 and 56 neurons (hereinafter referred to as NN300 and NN56) were applied to the 6-hr simulation, which corresponds to 7,200 accumulated model/radiation time steps at increments of 3 s. As mentioned previously, the main goal in this study is to investigate the applicability of NN-radiation emulator to weather forecasting model. For this purpose, frequent uses (i.e., every time step) of NN300 and NN56 are equivalent to infrequent uses of the original radiation scheme by 20 and 100 times (WRF20 and WRF100, with 60-s and 300-s radiation time steps, respectively) in terms of computational cost (Note that KLAPS over Korea is performing with the infrequent use of radiation scheme by 15 times). The accuracy of theses simulations was evaluated by considering the WRF control run to be true.

193 **3. Results**

194 The trained heating rate and flux results are shown in Fig. 1. Although the NN training
195 was designed to identify an optimized convergence solution for all given input-output pairs,
196 the explanation obtained from the inputs may vary depending on the characteristics of the
197 outputs. We note that the training results (in terms of R^2) for the heating rate profiles
198 (0.941516 for LW and 0.926777 for SW) are less accurate than those for the single-level
199 fluxes (0.999748 for LW and 0.997313 for SW), implying that vertical profiles involve
200 greater uncertainty than single-level products. The SW results exhibit lower R^2 and higher the
201 root mean squared error (RMSE) for fluxes than those of the LW. These results suggest that
202 SW processes are more complex than LW processes at the cloud-resolving scale. Some of the
203 uncertainty is presumed to be related to the excluded microphysics variables. However,
204 because the inclusion of microphysics variables did not show advantages in the significant
205 increase of accuracy despite of doubling computation cost in this study, its benefits need to be
206 comprehensively examined in the future real case simulation.

207 Figure 2 shows the vertical distribution of the horizontal (50 km) mean cloud fraction and
208 heating rate (LW and SW) with the accumulated forecast time for the WRF control run,
209 NN300, and WRF20. The experiment simulated a vertically developing cloud by initial
210 forcing of warm bubble heating at the lower center of the domain, following precipitation.
211 Hence, the cloud fraction as a key factor in determining radiative processes in this experiment.
212 Until about 20 min had elapsed, the negative LW and positive SW values were clearly
213 detected as the cloud grew to 9 km (Figs. 2b and c). Although initial cloud forcing occurred
214 mainly near the center of the domain, it was also identified in the 50-km mean feature
215 because of its strength. The cloud top, regarded as a 10% cloud fraction, developed up to 12
216 km for 2 hrs, but after that, the cloud top height decreased to 9 km (Fig. 2a). Areas with more
217 than 90% cloud fractions were present at an altitude of approximately 9 km on average at 2

hrs but lowered further to approximately 6.5 km after 6 hrs. Evolutionary features of the LW and SW heating rate profiles, the main outputs of the radiation parameterization, are shown in Figs. 2b and c. The strongest LW cooling area, above the high cloud fraction, was located over 9–12 km for 3 hrs but fell to 7–9 km within 6 hrs (Fig. 2b). The strongest SW warming was also found over the LW cooling area for the first 3 hrs (Fig. 2c). Similar LW cooling and SW warming feature responses to the cloud fraction were reported by Zhang et al. (2017). Although the LW cooling trend lasted up to 6 hrs, the SW warming weakened rapidly after 3 hrs because of reduced solar insolation at an increased zenith angle. Weak LW warming also appeared below the cloud layer, as well as near the surface, after 2 hrs.

The evolutionary feature of NN300, equivalent to twenty times speedup, exhibited good agreement with the control run, even during the latter part of the forecast time (middle row of Fig. 2). In relation to the upward development of clouds, the LW cooling and SW warming features within the first 30 min were accurately simulated (Figs. 2e–f). The strong LW cooling area present over 9–12 km within 3 hrs and 7–9 km at 6 hours was well represented in NN300 (Fig. 2e). The weak LW warming below the cloud and over the surface (Fig. 2e) and the strong SW warming area above 3 K day^{-1} (Fig. 2f) were also represented well. The WRF20 exhibited similar performance to the NN300 for large-scale features (Figs. 2g–i). However, Table 1 shows that the NN300 results agreed better with the control run (i.e., lower RMSE and higher R^2) than did the WRF20 results. Note that the mean biases were both close to zero, so the RMSE results may be the most appropriate measure of accuracy. We observed that, in terms of the RMSE, the accuracy of NN300 was improved by 19% for LHR, 22% for SHR, and 25% for the cloud fraction, relative to WRF20. The NN56, equivalent to a hundredfold speedup, yielded RMSE improvements of 24% for the LW heating rate, 11% for the SW heating rate, and 42% for the cloud fraction, in comparison to WRF100. Surprisingly, the NN56 results were even more accurate than the WRF20, despite the huge difference in

243 computation cost (i.e., a factor of 100 vs. 20 in speedup). These results suggest that the
244 frequent use of a radiation emulator can be beneficial in terms both computational speed and
245 accuracy, relative to the infrequent use of the original scheme, especially for severe weather
246 forecasting for which radiative processes at the cloud-resolving scale are important.

247 The upper panel of Fig. 3 shows evolutionary features in the horizontal domain (x) for
248 LW/SW fluxes, surface temperature (Ts), and precipitation for the control run. The total sky
249 LW upward flux at the TOA (LWUPT) exhibited a high value under the clear sky in the early
250 stages but rapidly decreased in relation to horizontally spread clouds (Fig.2a). Unlike the
251 LWUPT, total sky SW upward fluxes at the TOA (SWUPT) were greatly increased by cloudy
252 conditions but then gradually decayed until sunset. The LW and SW fluxes at the surface
253 (LWUPB, LWUPBC, LWDNB, LWDNBC, and SWUPB) developed into a horizontally
254 asymmetric pattern tilted in the positive x direction that decreased toward sunset. These
255 features are thought to be intimately related to Ts. Precipitation was mainly distributed over
256 the ±10- km area corresponding to the center of the clouds and appears to have been biased
257 toward the negative x direction after 5 hrs.

258 Both NN300 and WRF20 represent characteristic features found in the control run,
259 although difference exists from point to point (Fig. 3). Although the developed NN-emulator
260 inevitably includes the discrepancies, their differences are within reasonable limits, as listed
261 in Table 1. The NN300 exhibited improvements of 28% in LW fluxes and 20% in SW fluxes,
262 in terms of RMSE, compared to the WRF20. The improvements were mainly associated with
263 LWUPT, LWDNB, LWDNBC, SWUPT, and SWUPB, with the results for these exhibiting
264 the largest discrepancies with respect to the control run. In particular, NN56 exhibited a 23%
265 lower RMSE, compared to the LW fluxes of WRF20, implying advantages in both speed and
266 accuracy. The NN300 reasonably simulated areas with Ts greater than 298 K for up to 3 hrs
267 as well, but WRF20 does not provide this feature. Compared to WRF20, the Ts results from

NN300 and NN56 represent significant reductions in RMSE, i.e., 43% and 34%, respectively, as well as more accurate pattern correlations, i.e., 0.94 and 0.92, respectively. Precipitation is a bottleneck in prognostic forecasting since it is difficult to simulate accurately under conditions of higher uncertainty and complexity (relatively lower R^2 values in Table 1). Nevertheless, the NN300 results effectively represented the precipitation pattern, which was mainly concentrated at ±10 km in the control run (Fig. 3). However, WRF20 exhibited a heavy rainfall area up to the 20-km point, resulting in a huge difference with respect to the control run, especially after 4 hrs. For precipitation, the NN300 and NN56 results represented improvements of 25% and 21% in terms of reduced RMSE, in addition to an enhanced R^2 (0.58), in comparison to WRF20.

4. Summary and Conclusion

This study evaluated the forecast performance of NN-based radiation emulators at the cloud-resolving scale. For this purpose, NN-based RRTMG-K radiation emulators were developed with 300 and 56 neurons (NN300 and NN56) and implemented in the WRF model in the framework of an idealized two-dimensional squall-line simulation with 250-m spacing. A combined algorithm for LW and SW radiation was introduced for speedup and was integrated over 6 hrs at a 3-s time step. The emulator results appeared to reproduce well vertical evolutionary features of the LW/SW heating rate related to the cloud fraction. The prognostic features of LW/SW fluxes, surface temperature, and precipitation were also well simulated with the emulators. The NN300 and NN56 results were compared with those obtained from infrequent uses of RRTMG-K by 20 and 100 times with 60-s and 300-s radiation time steps (WRF20 and WRF100), equivalent to the same computational cost for NN300 and NN56, respectively, with the results for a WRF control run at a 3-s radiation time step considered to be true. The accuracy improvement achieved with NN300 (NN56), in

terms of RMSE, were 19% (24%) for LW heating rate, 22% (11%) for SW heating rate, 25% (42%) for cloud fraction, 28% (23%) for LW fluxes, 20% (16%) for SW fluxes, 43% (34%) for surface temperature, and 25% (21%) for precipitation, compared to those obtained with WRF20 and WRF100, respectively. The NN56 results were even more accurate than the WRF20 results, despite a 80% lower consumption of computational resources.

Since all previous studies on radiation emulators have applied to the climate simulations at horizontal resolutions of 100–300 km, the results of this study are particularly meaningful in that they represent the first attempt to evaluate the forecast performance of radiation emulators at the cloud-resolving scale, corresponding to strongly nonlinear condition. In particular, the validity of radiation emulation at the cloud-resolving scale is essential to forecasting severe weather accompanied by complex cloud systems. Furthermore, the evaluation method developed in this study (which achieves better performance than the infrequent use of the original radiation scheme, equivalent to similar speedup condition) provides insights that will be useful in the future development of radiation emulators. This is important because an emulator should provide benefits in speedup or accuracy in comparison to the infrequent radiation method. No previous research has presented an evaluation of radiation emulators under such strict conditions, because previous studies on radiation emulators were focused on imitating the original radiation scheme in climate simulations with coarse temporal resolutions (1–3 hrs). We acknowledge that the results obtained in this study apply to very limited ideal condition that cannot be easily generalized when applied to an actual case. Therefore, it will be necessary to ensure that the forecast performance (especially for severe weather) is truly improved by applying NN-based radiation emulators to real cases in the future.

Acknowledgements

We are deeply grateful to Dr. V. M. Krasnopolsky and A. Belochitski (NOAA/EMC) for providing the fortran-based NN software used in this study and their constructive comments. The WRF model used in this study was obtained from https://www2.mmm.ucar.edu/wrf/users. This work was funded by the KMA Research and Development Program "Development of the AI technique for the prediction of rainfall optimized over the Korean peninsula" under Grant (KMA2018-00124).

References

Bea, S. Y., and Park, R.-S. (2019). Consistency between the cloud and radiation processes in a numerical forecasting model, *Meteor. Atmos. Phys.*, 131, 1429–1436, https://doi.org/10.1007/s00703-018-0647-9.

Bea, S. Y., Hong, S.-Y., and Lim, K. S. S. (2016). Coupling WRF Double-Moment 6-Class microphysics schemes to RRTMG radiation scheme in Weather Research Forecasting model, *Adv. Meteor.*, 2016, 5070154, https://doi.org/10.1155/2016/5070154.

Bea, S. Y., Hong, S.-Y., and Tao, W.-K. (2019). Development of a Single-Moment Cloud Microphysics Scheme with Prognostic Hail for the Weather Research and Forecasting (WRF) Model, *Asia-Pac. J. Atmos. Sci.*, 55, 233–245, https://doi.org/10.1007/s13143-018-0066-3.

Baek, S. (2017), A revised radiation package of G-packed McICA and two-stream approximation: Performance evaluation in a global weather forecasting model, *J. Adv. Model. Earth Syst.*, 9, 1628–1640, https://doi.org/10.1002/2017MS000994.

Belochitski, A., Binev, P., DeVore, R., Fox-Rabinovitz, M., Krasnopolsky, V., and Lamby, P. (2011). Tree approximation of the long wave radiation parameterization in the NCAR CAM global climate model, *J. Comput. Appl. Mathmatic.*, 236, 447–460, https://doi.org/10.1016/j.cam.2011.07.013.

Brenowitz, N. D., and Bretherton, C. S. (2018). Prognostic validation of a neural network unified physics parameterization. *Geophys. Res. Lett.*, 45, 6289–6298. https://doi.org/10.1029/2018GL078510.

Chevallier, F., Chéruy. F., Scott, N. A., and Chédin, A. (1998). A neural network approach for a fast and accurate computation of a longwave radiative budget, *J. Appl. Meteor.*, 37, 1385–1397, https://doi.org/10.1175/1520-0450(1998)037.

Chevallier, F., Morcrette, J.-J., Chéruy, F., and Scott, N. A. (2000). Use of a neural-network-based long-wave radiative-transfer scheme in the ECMWF atmospheric model, *Quart. J. Roy. Meteor. Soc.*, 126, 761-776, https://doi.org/10.1002/qj.49712656318.

Clough, S. A., Iacono, M. J., & Moncet, J.-L. (1992). Line-by-line calculation of atmospheric fluxes and cooling rates: Application to water vapor, *J. Geophys. Res.*, 97, 15761–15785, https://doi.org/10.1029/92JD01419.

Clough, S. A., Shephard, M. W., Mlawer, E. J., Delamere, J. S., Iacono, M. J., Cady-Pereira, K., Boukabara, S., and Brown, P. D. (2005). Atmospheric radiative transfer modeling: a summary of the AER codes, *J. Quant. Spectrosc. Radiat. Transfer*, 91, 233–244, https://doi.org/10.1016/j.jqsrt.2004.05.058.

Gentine, P., Pritchard, M., Rasp, S., Reinaudi, G., and Yacalis, G. (2018). Could machine learning break the convection parameterization deadlock? *Geophys. Res. Lett.*, 45, 5742–5751. https://doi.org/10.1029/2018GL078202.

Gu, Y., Liou, K. N., Ou, S. C., and Fovell. R. (2011), Cirrus cloud simulations using WRF with improved radiationparameterization and increased vertical resolution, *J. Geophys. Res.*, 116, D06119, https://doi.org/10.1029/2010JD014574.

Hong, S.-Y., Kwon, Y. C., Kim, T.-H., Kim, J.-E., Choi, S.-J., Kwon, I.-H., Kim, J., Lee, E.-H., Park, R.-S., and Kim, D.-I. (2018). The Korean Integrated Model (KIM) system for weather forecasting. *Asia-Pac. J. Atmos. Sci.*, 54, 267–292, https://doi.org/10.1007/s13143-018-0028-9

Iacono, M. J., Delamere, J. S., Mlawer, E. J., Shephard, M. W., Clough, S., A., and Collins, W., D. (2008). Radiative forcing by long-lived greenhouse gases: Calculations with the AER radiative transfer models, *J. Geophys. Res.*, 113, D13103, https://doi.org/10.1029/2008JD009944.

Kim, Y.-S., Park, O.-R., and Hwang, S.-O. (2002). Realtime operation of the Korea Local Analysis and Prediction System at METRI, *Asia-Pac. J. Atmos. Sci.*, 38, 1–10.

Kopparl, P., Natraj, V., Spurr, R., Shia, R.-S., and Crisp, D. (2016). A fast and accurate PCA based radiative transfer model: Extension to the broadband shortwave region, *J. Quant. Spectrosc. Radiat. Transfer*, 173, 65–71, http://dx.doi.org/10.1016/j.jqsrt.2016.01.014.

Krasnopolsky, V., and Fox-Rabinovitz, M. S. (2006). Complex hybrid models combining deterministic and machine learning components for numerical climate modeling and weather prediction, *Neural Networks*, 19, 122–134, https://doi.org/10.1016/j.neunet.2006.01.002.

Krasnopolsky, V., Fox-Rabinovitz, M. S., and Chalikov, D. V. (2005). New approach to calculation of atmospheric model physics: Accurate and fast neural network emulation of longwave radiation in a climate model, *Mon. Weather Rev.*, 133, 1370–1383, https://doi.org/10.1175/MWR2923.1.

Krasnopolsky, V., Fox-Rabinovitz, M. S., and Belochitski, A. A. (2008a). Decadal climate simulations using accurate and fast neural network emulation of full, longwave and shortwave, radiation, *Mon. Weather Rev.*, 3683–3695, https://doi.org/10.1175/2008MWR2385.1.

Krasnopolsky, V., Fox-Rabinovitz, M. S., Tolman, H. L., and Belochitski, A. A. (2008b). Neural network approach for robust and fast calculation of physical processes in numerical environmental models: Compound parameterization with a quality control of

larger errors, *Neural Networks,* 21, 535–543, https://doi.org/10.1016/j.neunet.2007.12.019.

Krasnopolsky, V., Fox-Rabinovitz, M. S., Hou, Y. T., Lord, S. J., and Belochitski, A. A. (2010). Accurate and fast neural network emulations of model radiation for the NCEP coupled Climate Forecast System: Climate simulations and seasonal predictions, *Mon, Weather Rev., 138*, 1822–1842, https://doi.org/10.1175/2009MWR3149.1

Krasnopolsky, V., Fox-Rabinovitz, M. S., and Belochitski, A. A. (2013). Using ensemble of neural networks to learn stochastic convection parameterizations for climate and numerical weather prediction models from data simulated by a cloud resolving model, *Adv. Artif. Neural Sys.*, 2013, 485913, https://doi.org/10.1155/2013/485913.

Lim, K.-S. S., and Hong, S.-Y. (2010). Development of an effective double-moment cloud microphysics scheme with prognostic Cloud Condensation Nuclei (CCN) for weather and climate models, *Mon, Weather Rev.,* 138, 1587–1612, https://doi.org/10.1175/2009MWR2968.1.

Pauluis, O., and Emanuel, K. (2004). Numerical instability resulting from infrequent calculation of radiative heating, *Mon, Weather Rev.,* 132, 673–686, https://doi.org/10.1175/1520-0493(2004)132.

Pal, A., Mahajan, S., and Norman, M. R. (2019). Using deep neural networks as cost-effective surrogate models for Super-Parameterized E3SM radiative transfer, *Geophys. Res. Lett.*, 46, 6069–6079, https://doi.org/10.1029/2018GL081646.

Pincus, R., and Stevens, B. (2013). Paths to accuracy for radiation parameterizations in atmospheric models, *J. Adv. Model. Earth Syst.,* 5, 255–233, https://doi.org/10.1002/jame.20027.

Rasp, S., Pritchard, M. S., and Gentine, P. (2018). Deep learning to represent subgrid processes in climate models, *Proc. Nat. Acad. Sci.,* 115, 9684–9689, http://www.pnas.org/cgi/doi/10.1073/pnas.1810286115.

Scher, S. (2018). Toward data-driven weather and climate forecasting: Approximating a simple general circulation model with deep learning, *Geophys. Res. Lett.*, 45, 12616–12622, https://doi.org/10.1029/2018GL080704.

Song, H.-J., Sohn, B. J., Hong, S.-Y., and Hashino, T. (2017). Idealized numerical experiments on the microphysical evolution of warm-type heavy rainfall. *J. Geophys. Res. Atmos.*, 122, 1685–1699, https://doi.org/10.1002/2016JD02563.

Wang, J., Balaprakash, P., and Kotamarthi, R. (2019). Fast domain-aware neural network emulation of a planetary boundary layer parameterization in a numerical weather forecast model, *Geosci. Model Dev.,* 12, 4261–4274, https://doi.org/10.5194/gmd-12-4261-2019.

Xu, K.-M., and Randall, D. A. (1995). Impact of interactive radiative transfer on the macroscopic behavior of cumulus ensembles. Part I: radiation parameterization and sensitivity tests, *J. Atmos. Sci.,* 52, 785–799, https://doi.org/10.1175/1520-0469(1995)052.

Zhang, K., Randel, W. J., and Fu, R. (2017). Relationships between outgoing longwave radiation and diabatic heating in reanalyses, *Clim. Dyn.*, 49, 2911–2929, https://doi.org/10.1007/s00382-016-3501-0.

Table 1. Evaluations results for NN-emulators using 300 and 56 neurons (NN300 and NN56) and infrequent radiation time steps by 20 and 100 times (WRF20 and WRF100) versus the WRF control run. The statistics in the table are the root mean squared error (RMSE) and the square of the correlation coefficient (in parentheses) relative to the control run.

Experiments	NN300	WRF20	NN56	WRF100
Speedup of radiation	20.76	20	100.81	100
Reduced computation time	82.12%	82.03%	85.96%	85.64%
LW heating rate [K day^{-1}]	0.92 (0.92)	1.14 (0.88)	1.03 (0.90)	1.35 (0.83)
SW heating rate [K day^{-1}]	0.40 (0.90)	0.51 (0.84)	0.47 (0.86)	0.53 (0.83)
Cloud fraction [%]	6.04 (0.97)	8.04 (0.95)	6.27 (0.97)	10.86 (0.91)
LW flux [W m^{-2}]	5.68 (1.00)	7.97 (0.99)	6.15 (1.00)	8.03 (0.99)
LWUPT	10.90 (0.91)	13.55 (0.87)	11.49 (0.87)	15.13 (0.84)
LWUPTC	1.86 (0.86)	2.85 (0.71)	2.18 (0.80)	3.22 (0.71)
LWUPB	1.03 (0.85)	1.56 (0.68)	1.13 (0.81)	1.41 (0.76)
LWUPBC	0.72 (0.97)	1.31 (0.89)	0.96 (0.91)	1.12 (0.94)
LWDNB	6.84 (0.84)	10.42 (0.66)	7.19 (0.82)	9.42 (0.74)
LWDNBC	4.78 (0.97)	8.76 (0.88)	6.06 (0.92)	7.44 (0.94)
SW flux [W m^{-2}]	38.58 (0.99)	48.52 (0.99)	46.79 (0.98)	59.36 (0.97)
SWUPT	53.27 (0.97)	66.70 (0.95)	64.76 (0.95)	81.59 (0.93)
SWUPB	11.78 (0.96)	16.11 (0.93)	13.62 (0.94)	19.74 (0.90)
Surface temperature (T_s) [K]	0.92 (0.94)	1.62 (0.83)	1.07 (0.92)	1.78 (0.88)
Precipitation [mm]	0.19 (0.58)	0.24 (0.36)	0.18 (0.58)	0.21 (0.51)

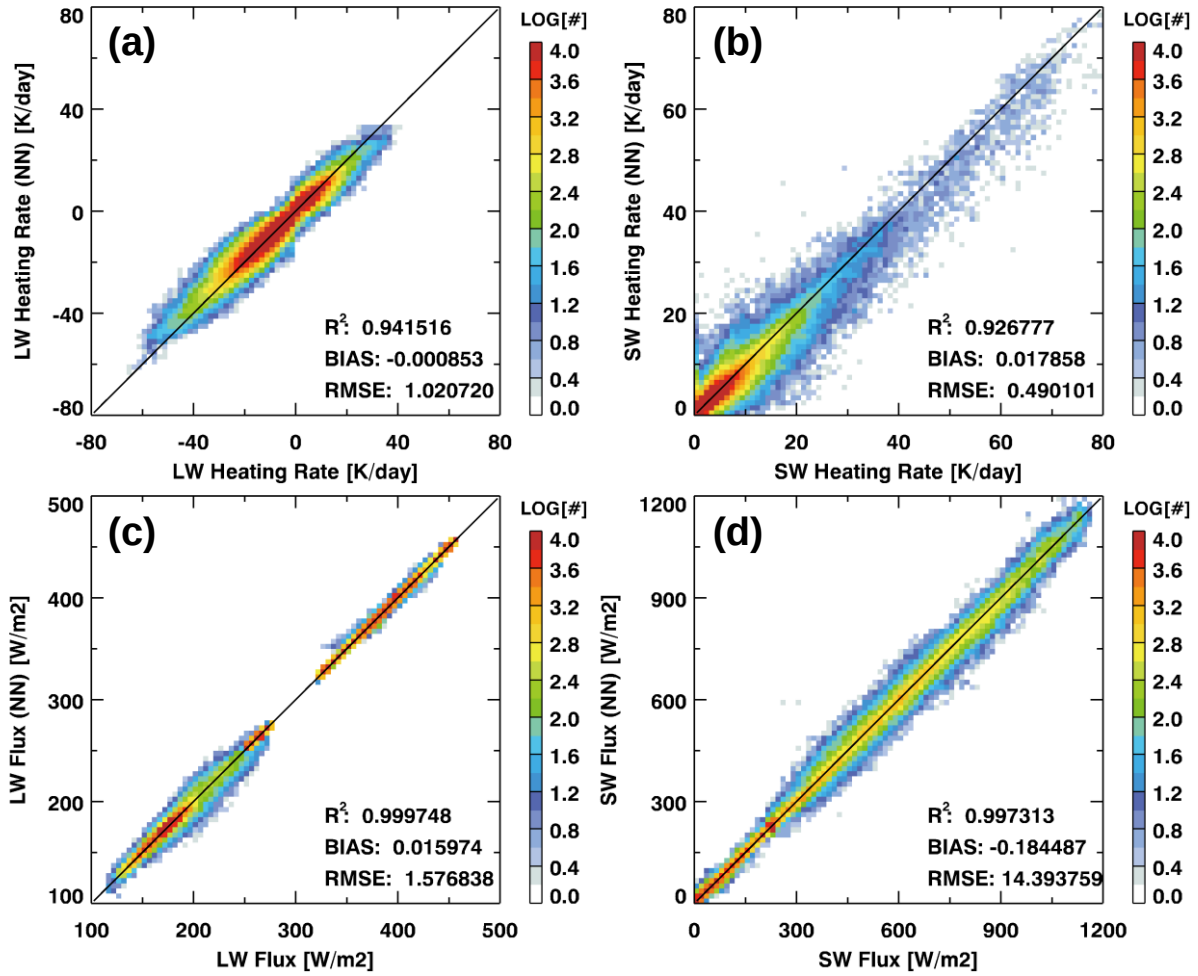

Figure 1. Comparison of (a) LW heating rate, (b) SW heating rate, (c) LW flux, and (d) SW flux between the control run and NN emulation with 300 neurons for training datasets. Heating rates for 39 vertical layers and six LW and two SW fluxes are expressed together in the figure. The colors in the figure represent the occurrence frequency on a log scale.

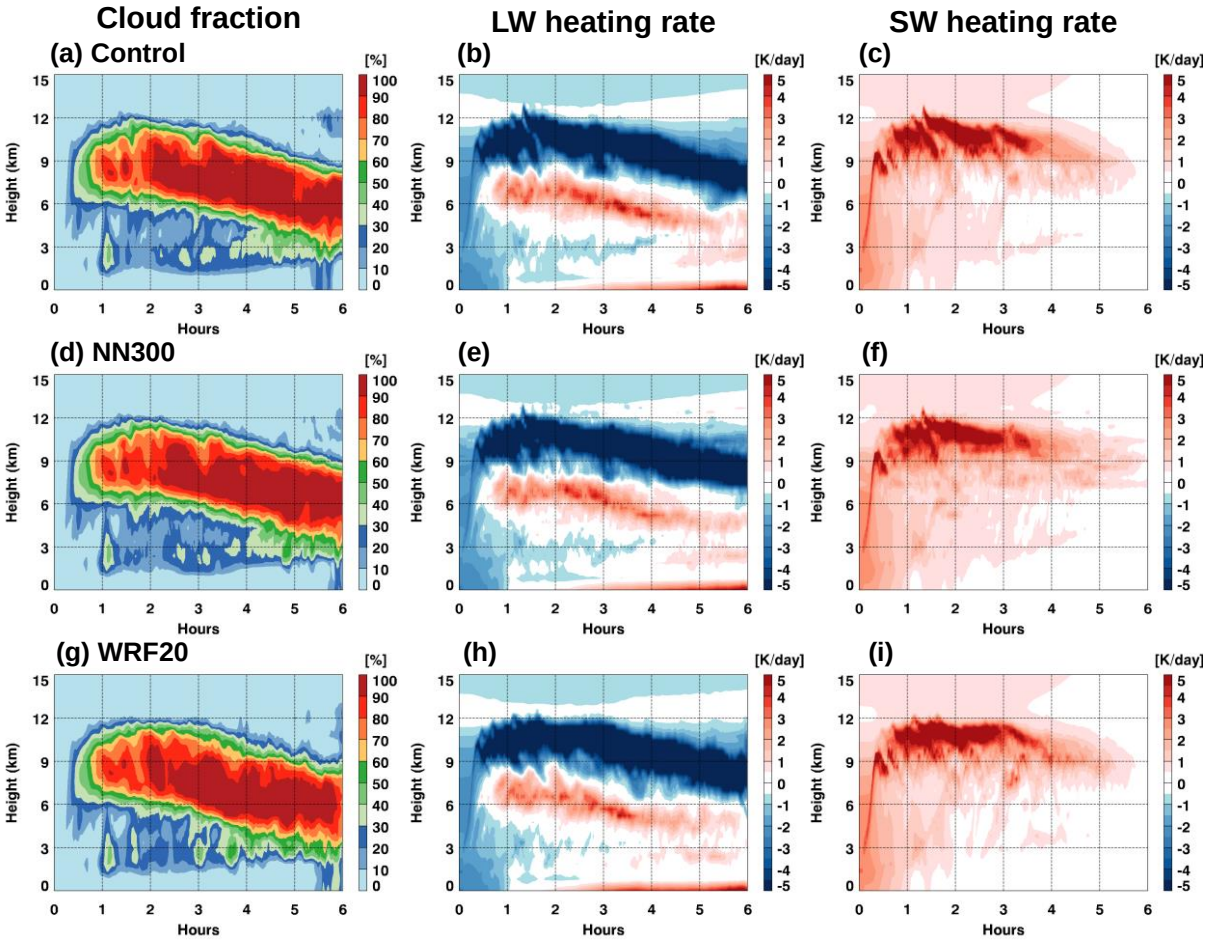

Figure 2. Temporal variation of 50-km mean (a) cloud fraction, and (b) LW and (c) SW heating rate profiles for the control run. (d–f) Same as (a–c) but for the WRF simulation using the NN-emulator with 300 neurons (NN300). (g–i) Same as (a–c) but for the WRF simulation with the infrequent radiation time step by 20 times (WRF20).

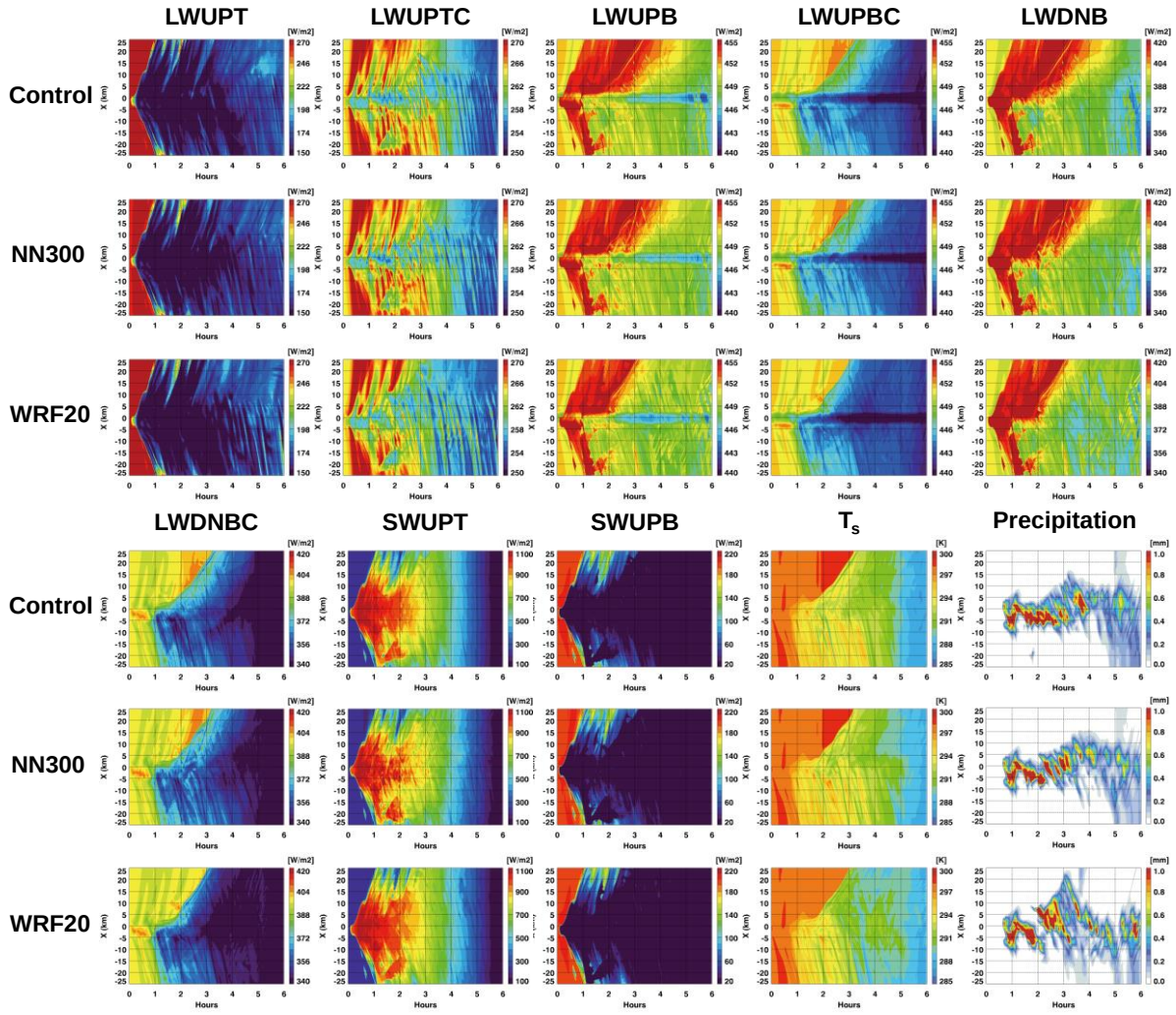

456
457 **Figure 3.** Temporal and spatial variation of LW and SW fluxes, surface temperature (T_s), and
458 precipitation for the control run (top panel), NN300 (middle panel), and WRF20 (bottom
459 panel). LW, SW, UP, DN, T, B, and C indicate longwave, shortwave, upward, downward, top
460 of atmosphere, bottom of atmosphere, and clear sky, respectively.

461